Journal of Materials Chemistry A

ROYAL SOCIETY OF CHEMISTRY

PAPER

View Article Online
View Journal | View Issue

Cite this: J. Mater. Chem. A, 2023, 11, 17045

Elucidating the oxygen reduction reaction kinetics on defect engineered nanocarbon electrocatalyst: interplay between the N-dopant and defect sites†

Sakshi Bhardwaj,[a] Samadhan Kapse,[b] Soirik Dan,[c] Ranjit Thapa*[b] and Ramendra Sundar Dey*[a]

Received 14th February 2023
Accepted 6th April 2023

DOI: 10.1039/d3ta00871a

rsc.li/materials-a

The active sites of electrocatalysts play a crucial role in the material design and mechanistic exploration of an electrocatalytic reaction. Defect-tailored heteroatom-doped carbon-based electrocatalysts for oxygen reduction reaction (ORR) have been much explored, but there is ambiguity in the prediction of active sites responsible for the performance of the material. To find the origin of the activity of this class of catalysts towards ORR, in this work, we use the quantum mechanics/machine learning (QM/ML) approach to derive energy-optimized models with both N-atoms and 5-8-5 defect sites which manifest exemplary ORR activity. Following this approach, we synthesized defect-engineered graphene (DG) using the zinc template method at 1050 °C to achieve optimum N-dopants and intrinsic (5-8-5) defects. The obtained electrocatalyst exhibits hierarchical porosity, high surface area, low nitrogen content, good stability and a satisfying ORR performance with a half-wave potential ($E_{1/2}$) of 0.82 V, comparable to that of commercial Pt/C ($E_{1/2}$ = 0.82 V). Further, the full energy profile was deduced using density functional theory and the charge redistribution in the material cross-verified a reduced overpotential for ORR. This work provides a strategy for the synthesis of noble-metal-free high-performance electrocatalysts for energy conversion.

Introduction

The oxygen reduction reaction (ORR) is the pivotal cathodic reaction in fuel cells and metal-air batteries, which are considered promising sources of clean renewable energy due to their high energy conversion efficiency, cleanliness and sustainability.[1] Noble metal platinum (Pt)-based electrocatalysts are considered state-of-art catalysts for ORR[2] but are limited in wide commercial applications due to their exorbitant cost, scarce resources, low fuel crossover and poor long-term stability.[3] Thus, extensive research is being done to replace Pt-based catalysts by (1) reducing the particle size of Pt for its utilization in cluster or atomic form or alloying Pt to minimize Pt usage,[4,5] (2) developing non-noble transition metal electrocatalysts to completely replace Pt[6] and (3) exploring metal-free electrocatalysts that present comparable/better activity for ORR.[7] However, transition metal-based electrocatalysts are always accompanied by several drawbacks, such as poor durability, lower selectivity, susceptibility to gas poisoning and adverse environmental impacts.[8,9] In contrast, the distinctive structural diversity of nanocarbon-based metal-free electrocatalysts and their various advantageous features, such as high abundance, good physico-chemical stability, remarkable activity, high electrical conductivity, low cost, and environmental friendliness, make them highly regarded candidates for ORR.[10]

Pure graphene is non-polar, lacks active sites and shows poor electrochemical activity.[11] Therefore, numerous strategies have been adopted to improve its electrocatalytic properties.[11–13] Defect engineering in carbon nanomaterials is considered one of the most effective methods.[14–17] According to the second law of thermodynamics,[18,19] crystalline materials will always have lattice imperfections or disorder arising from the production process or impurities. The presence of atomic disorder or defects is the origin of the electronic, optical and mechanical properties of carbonaceous matrices. It is well known that the presence of heteroatoms including N, P, S, B and O (extrinsic defects) and topological defects (intrinsic defects) in nanocarbon materials is responsible for the disturbance in the local electronic structure that influences the charge distribution in the framework and results in improved electrocatalytic performance of the carbonaceous materials towards ORR.[20,21] Moreover, the presence of N and defects in the sp^2 framework cause alteration in the charge and spin distribution of the carbon framework, which facilitates the adsorption of oxygen

[a]Institute of Nano Science and Technology (INST), Sector-81, Mohali-140306, Punjab, India. E-mail: rsdey@inst.ac.in

[b]Department of Physics, SRM University, Andhra Pradesh 522240, India

[c]Indian Association for the Cultivation of Science, Kolkata 700032, India

† Electronic supplementary information (ESI) available. See DOI: https://doi.org/10.1039/d3ta00871a

molecules, reduces the energy barrier, subsequently leads to the breaking of the O–O bond and improves the overall reaction rate.[22,23] Nonetheless, there is still controversy in the literature questioning which of graphitic-N,[23,24] pyridinic-N[25,26] or topological defects is the true active site for ORR when they all are present in carbonaceous matrices. Nitrogen-doped nanocarbon materials have gained massive attention, with various studies showing good electrocatalysis,[27,28] after the report on nitrogen-doped carbon nanotube arrays for ORR from Dai's group.[29] Intrinsic defects have been ignored for a long time during research progress into the ORR mechanism, but have now become a point of focus due to their significant contribution towards advanced ORR activity.[30,31] Most literature has some solution for choosing active sites, but the design of the active sites is based on proof-of-concept research. Therefore, an efficient principle is required for the screening of carbon catalysts. For this, descriptors in combination with machine learning (ML) algorithms is a good approach to narrow down the ideal models for catalysts.[32–35] Then, in the selected models, a predictive model can be used to find those with a higher number of active sites.[31] This approach helps to narrow down the search for a catalyst and suggest the best possible active material to synthesize in the laboratory.

In this work, we have considered distinct types of models with N-content and defects. In a previous study, the 5-8-5 defect proved to be more active for ORR. Our main concern is to find the active sites within models having both N-content and the 5-8-5 defect. Using the QM/ML approach, we screened the models and narrowed the choices down to three models (I, II and III) with optimum N-content and 5-8-5 defects (Fig. 1a–c) and their active sites were determined for efficient ORR. Following this theoretical investigation, we have synthesized a N-doped and 5-8-5 defect-enriched graphene-like material (DG-*T*) by pyrolysis of C and N sources in the presence of a porogen at three different temperatures. The catalyst prepared at 1050 °C (DG-1050) possesses an optimal amount of defects and N-content. The presence of N-dopants and defects was evidenced by XPS and STM studies. The synergistic impact of both these defects is shown in the $E_{1/2}$ potential for ORR of 0.82 V, very close to that of commercial Pt/C (0.829 V); it also achieved excellent stability. In both the theoretical and experimental results, DG-1050 is found to be most active towards ORR with the maximum number of active sites. Next, a full energy pathway was done for this material. We found that N present in the vicinity of an intrinsic defect (5-8-5) synergistically plays a critical role in the activity origin of the nanocarbon catalyst. This work sheds light on the method of developing metal-free carbon-based

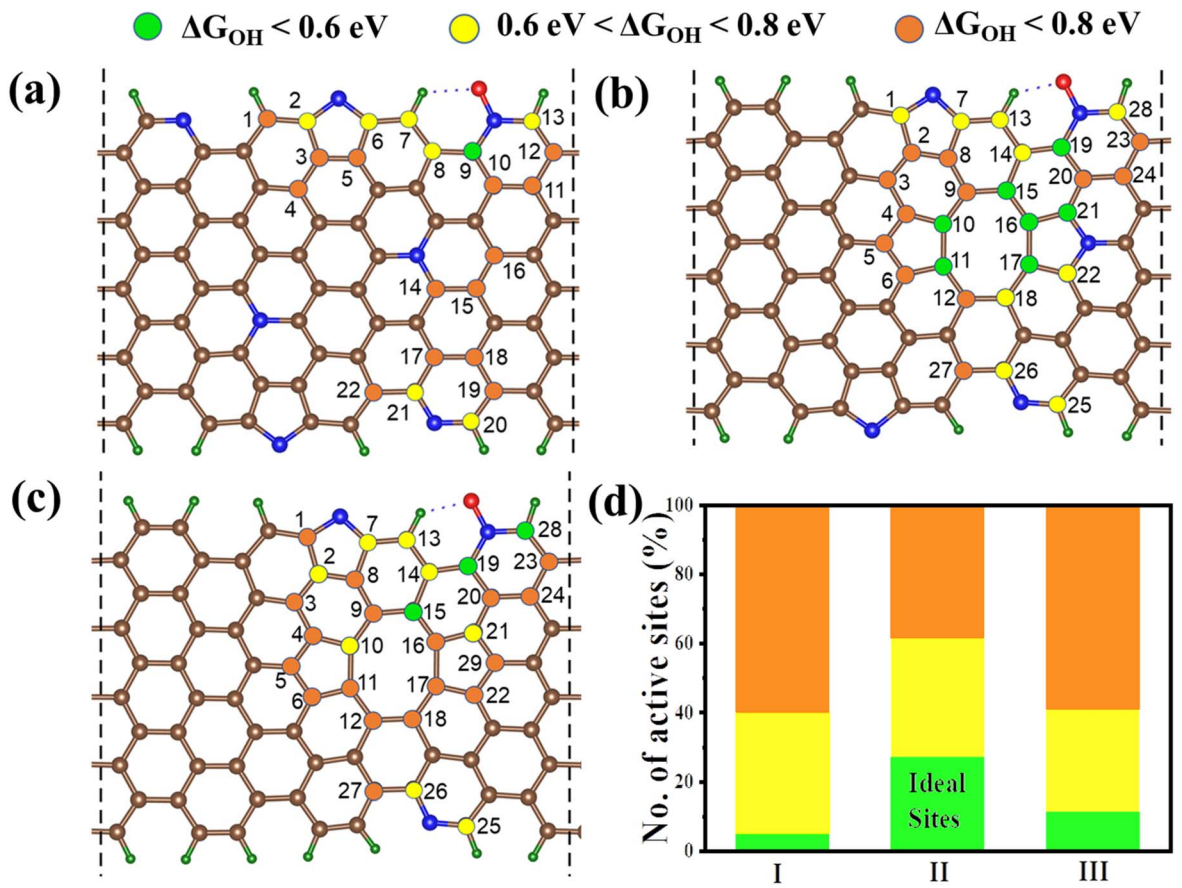

Fig. 1 Model structures of systems (a–c) I, II, and III. The numbers indicate each possible carbon active site in the structures. The red, blue, wine, and green colour spheres represent oxygen, nitrogen, carbon and hydrogen atoms, respectively. Filled circles with green, yellow and orange colours denote different ranges of ΔG_{OH} values. (d) The histogram for the percentage of active sites different ΔG_{OH} values in systems I, II, and III.

electrocatalysts by tuning the content of defects and N-dopants for their efficient usage in electrocatalytic applications.

Results and discussion

Various doping and defect-based configurations are feasible in carbon surfaces and, hence, a number of active sites can be possible, making it difficult to investigate for catalytic applications using conventional methods. Therefore, we need to screen these huge numbers of configurations rapidly to design an efficient carbon catalyst for ORR. Theoretically, the free energy profile is important in understanding the catalytic properties of materials; however, it requires adsorption calculations with enormous computational cost. In our previous works,[36–38] we reported different types of graphene model structures, including N-doped graphene, defective graphene, pyridinic-N, pyrrolic-N, oxidized-N, *etc.*, and then derived a predictive equation using the QM/ML approach to identify the ORR activity of any unknown random surface. We employed the π electronic descriptors of graphene surfaces in the machine learning algorithms and developed the efficient support vector regression (SVR) predictive model of OH adsorption energy (G_{OH}).[39]

This QM/ML approach is faster, more efficient and can help analyze any type of graphene-based configuration for ORR without performing adsorption calculations. Previous reports[40,41] suggest that machine learning in combination with DFT can accurately find the sites which are responsible for the activity. However, until now there have been no reports, to the best of our knowledge, wherein machine learning and DFT were performed on defect-enriched N-doped graphene to find the true active sites for ORR. Nitrogen doped in carbon systems has already been reported as an active dopant for ORR. Through the QM/ML approach, herein, we discover the specific roles of N-doping and defects towards the formation of active sites for ORR (Fig. S1†). Among them, the 5-8-5 defect more effectively decreases the charge neutrality to increase active sites on the graphene surface.[42] Based on the previous reports and our study on N-doping and the 5-8-5 defect, we modeled three realistic, random complex model structures termed systems I, II and III, as seen in Fig. 1. Model structure I is made with two pyrrolic-N, two pyridinic-N, two oxidized-N and two graphitic-N sites; model structure II is made with one pyrrolic-N, two pyridinic-N, one oxidized-N, one graphitic-N and a 5-8-5 defect; model structure III is made with one pyrrolic-N, one pyridinic-N, one oxidized-N and a 5-8-5 defect. For each system, the possible carbon active sites around the N-dopants and defects were selected for ORR study. Different types of energy, electronic and structural descriptors have been reported to define the ORR activity in carbon materials.[43–49] Most of these descriptors have limitations, such as lower efficiency, inability to predict the site-specific activity, *etc.* In this context, the change in Gibbs free energy of OH adsorption (ΔG_{OH}) is a well-known energy descriptor that effectively predicts site-specific ORR activity.[4,50] From the volcano correlation between ΔG_{OH} and thermodynamic overpotential (η), a value of ΔG_{OH} near zero indicates a smaller η and higher ORR activity.[75] Recently, the role of the π orbital of an active site in a carbon system has also been identified as an origin with electronic descriptors to predict site-specific catalytic activity for ORR.[51] Further, these π-orbital based descriptors ($D_\pi(E_F)$, R-O_π) have been used as features in machine learning algorithms to develop a highly cost effective (less computational power) predictive model ($\Delta G_O - \Delta G_{OH}$) OER application.[52] As for ORR, these electronic descriptors have been utilized in various machine learning algorithms to develop a predictive model of ΔG_{OH}.[39] Here, the predictive model of ΔG_{OH} is also calculated by using the simple linear fit method (Fig. S2†). The calculations for the simple linear fit method are given in Section S1a.† Among all the models, the SVR predictive model showed optimal performance and a higher test R^2 score (0.87) in 5-fold cross-validation (Fig. S3, Sections S1b and c†). This SVR predictive model of ΔG_{OH} is faster and more cost effective, requiring only a single DFT calculation for a carbon system to predict the ORR activity of all the sites (the Python code script is given in Section S1d†). Without the SVR model, we would need to perform three DFT calculations for O, OH and OOH intermediate adsorption on each active site to compute the ORR performance of each site. Therefore, we used this reported SVR predictive model to analyze the active sites in systems I, II and III for ORR.

Fig. 1a represents the 22 different possible carbon active sites of model I. To find the theoretical overpotentials on 22 sites, we would need to do 66 DFT calculations (three intermediates for each site), which require resources and time. But, by applying our SVR model, we can predict the ΔG_{OH} values and overpotential for these active sites by doing single DFT calculations of the host surface only. The story is the same for the other two models. So, the predictive model developed using the QM/ML approach and fewer DFT calculations helped us to find the best active site in a very efficient way. We found that in model I, the carbon site denoted as number 9 in Fig. 1a adjacent to the oxidized nitrogen shows the lowest ΔG_{OH} (0.53) and is the most active site for ORR in this model structure[53] (Table S1†), whereas the ΔG_{OH} values for seven other sites are in the range of 0.6 eV to 0.8 eV and fourteen sites show higher ΔG_{OH} values (>0.8 eV). As shown in Fig. 1b, model II has a 5-8-5 defect with a lower N-doping concentration compared to model I. Here, we observed that the combined effect of the 5-8-5 defect and N doping decreases the charge neutrality on graphene and creates more active sites with lower ΔG_{OH} values (<0.6 eV) for ORR (Table S2†). In model II, we found seven ideal active sites for ORR near 5-8-5 defects. In the case of the model III defective graphene (Fig. 1c), it is noted that the further decrease of N-doping percentage reduces the number of ideal active sites near 5-8-5 defects (Table S3†). In Fig. 1d, for easy understanding, we display a histogram using the percentage of active sites with different ΔG_{OH} ranges in models I, II and III. Therefore, we predict that the 5-8-5 defect and N doping play a combined role to improve the ORR performance in graphene systems.

Following the theoretical study, we synthesised the samples $DG_{x:y}$-T (T = pyrolysis temperature, $x:y$ = the ratio of melamine and zinc catalysts), as shown schematically in Fig. 2a. The experimental details are mentioned in the Experimental

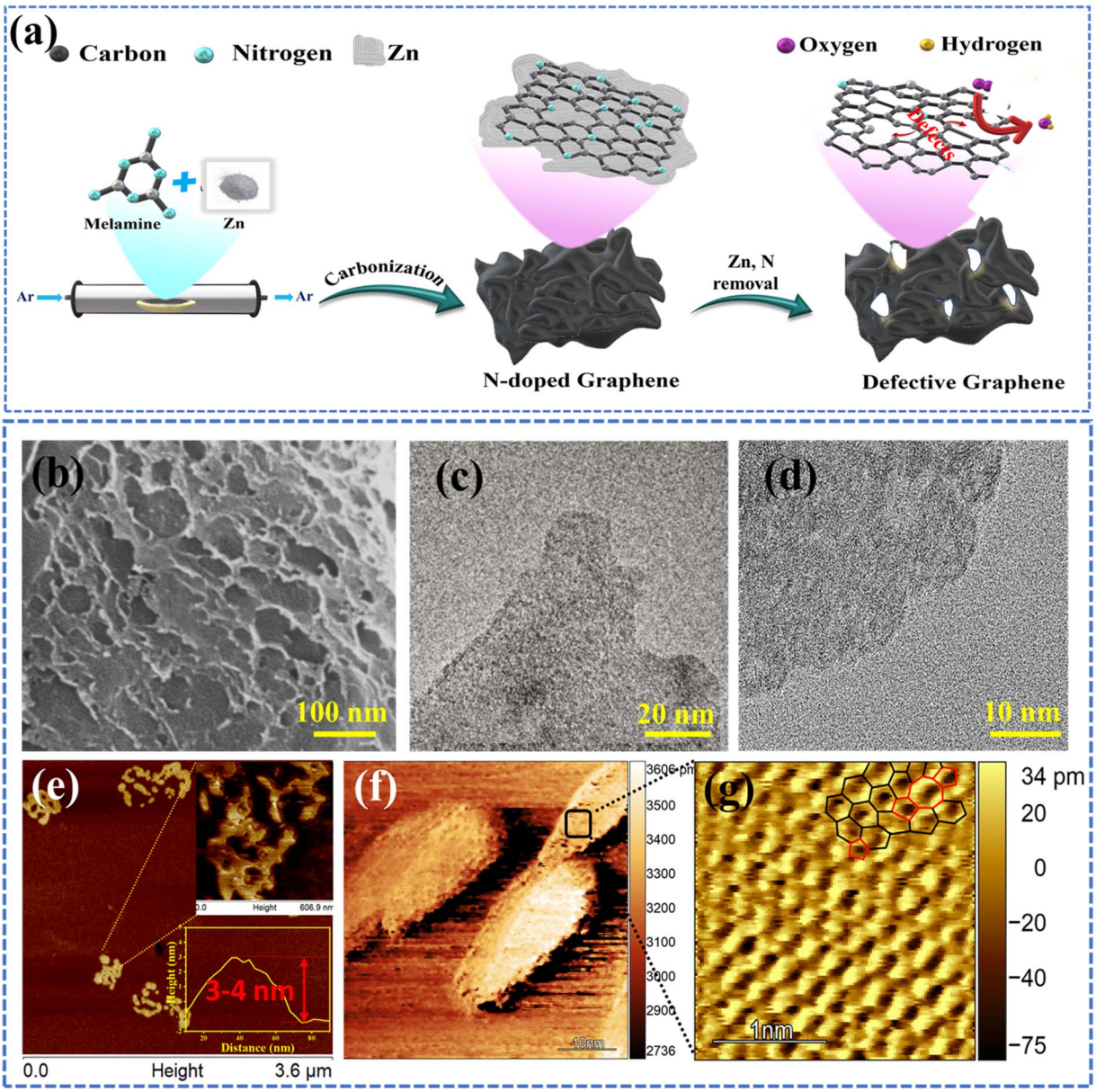

Fig. 2 (a) Schematic illustration of synthesis of $DG_{1:1}$-1050; (b) SEM image; (c and d) HRTEM images; (e) AFM image, inset: height profile graph; (f and g) STM images of $DG_{1:1}$-1050.

section. Briefly, DG was prepared by the pyrolysis of melamine and zinc dust in a particular ratio. Due to its alternating carbon and nitrogen atoms and powerful self-condensation capacity, melamine was selected as the carbon and nitrogen source to prepare DG. In this synthesis procedure, Zn not only serves as a template, but also acts as a porogen to construct a highly cross-linked 3D porous network structure, since Zn can be evaporated >907 °C during the carbonization process.[22,54] During the carbonization step at 800 °C, metallic Zn embeds into the carbon matrix and leads to the expansion of carbon layer distance. Further heating was performed at different temperatures (950, 1050, 1150 °C) to remove zinc and nitrogen to create defects.[22,55] Subsequently, the carbon atoms rearrange and self-organize themselves to form a carbon framework. Using only the carbon source dextrose, a defective carbon sample ($C_{1:1}$) was also prepared to check the effect of N on the ORR activity.

Field emission scanning electron microscopy (FESEM) and transmission electron microscopy (TEM) were used to analyse the morphology of the prepared samples. FESEM images (Fig. 2b) show a highly porous interconnected 3D network of graphene sheets that offers high specific surface area with a greater number of active sites to help in easy mass transport. The formation of flake-like wrinkled defective graphene sheets after carbonization at high temperature was confirmed by TEM (Fig. S4†). The edge defects produced by the removal of Zn[56,57] can be clearly seen in the high-resolution TEM (HRTEM) images (Fig. 2c and d). No usual graphitic lattices were found,

suggesting the disordered and defect-rich character of $DG_{1:1}$-1050. The associated selected area electron diffraction (SAED) pattern (inset Fig. S4†) displayed the two typical rings, (002) and (101), that correspond to the amorphous nature of $DG_{1:1}$-1050. Atomic force microscopy (AFM) evidenced the formation of ultrathin graphene sheets (Fig. 2e inset; height profile: ~3–4 nm) with localised destruction due to the removal of N and Zn atoms from the framework (Fig. 2e). The created intrinsic defects can be pentagons, heptagons, even octagons and holes *etc.*, formed by the rearrangement of atoms due to multiple single-atom or diatom vacancies created after the removal of N atoms.[58] Scanning tunnelling microscopy (STM) was used to visualize the defects formed in the synthesised material. Fig. 2f shows the low magnification image presenting the $DG_{1:1}$-1050 sheet; its highly resolved image (Fig. 2g) obtained at 1 nm clearly presents the various structural defects such as pentagons and 5-8-5 defects. These defects cause the local modulation of the electronic environment responsible for enhancing the electrocatalytic activity.

The X-ray diffraction (XRD) patterns for the different DG-*T*s (Fig. 3a) exhibited one broad characteristic peak at 24.8° and another small hump around 44° indexed to the (002) and (101) planes of nanocarbon, respectively, suggesting an amorphous structure with a low degree of graphitization that is expected to be beneficial for the electrocatalytic activity of the catalyst. Raman analysis is the most widely used tool to identify the degree of graphitization. The introduction of defects in carbon nanomaterials in the form of heteroatom doping or vacancies gives rise to an increase in the D-band (1337 cm^{-1}) intensity due to disruption of the hexagonal rings.[59,60] The G-band at 1569 cm^{-1} is attributed to the C–C and C–N bond vibrations of E_{2g} mode in sp^2-bonded graphitic carbon. These two characteristic peaks were obtained in all three $DG_{1:1}$-*T* samples (Fig. 3b). The intensity ratio of the D-band to the G-band (I_D/I_G) estimates the defect level present in carbon materials.[15,61] The I_D/I_G ratios were 1.05, 1.11, and 1.18 for $DG_{1:1}$-950, $DG_{1:1}$-1050 and $DG_{1:1}$-1150, respectively, showing that all the materials contained a high degree of carbon disorder. There was substantial decrease in N-content with increasing temperature and, thus, the surge in I_D/I_G ratio distinctly proves the extensive formation of defective domains. The abundant edge and topological defects along with the optimal N-content attuned the surface and electronic properties of $DG_{1:1}$-1050 that regulate the adsorption energies of electrocatalysis steps. The defect density present in the sp^2 domains of the graphene rose from 3.14×10^{11} to 3.54×10^{11} with increasing temperature, as calculated using the formula

$$n_d = (2.4 \times 10^{22}) \times \lambda_L^{-4} \times \frac{I_D}{I_G} \quad (1)$$

where n_d is the defect density (cm^{-2}) of the catalyst and λ_L is the wavelength (532 nm) used in Raman spectroscopy.[62]

Although Raman spectroscopy helps define the relationship between defects and ORR performance, it does not provide

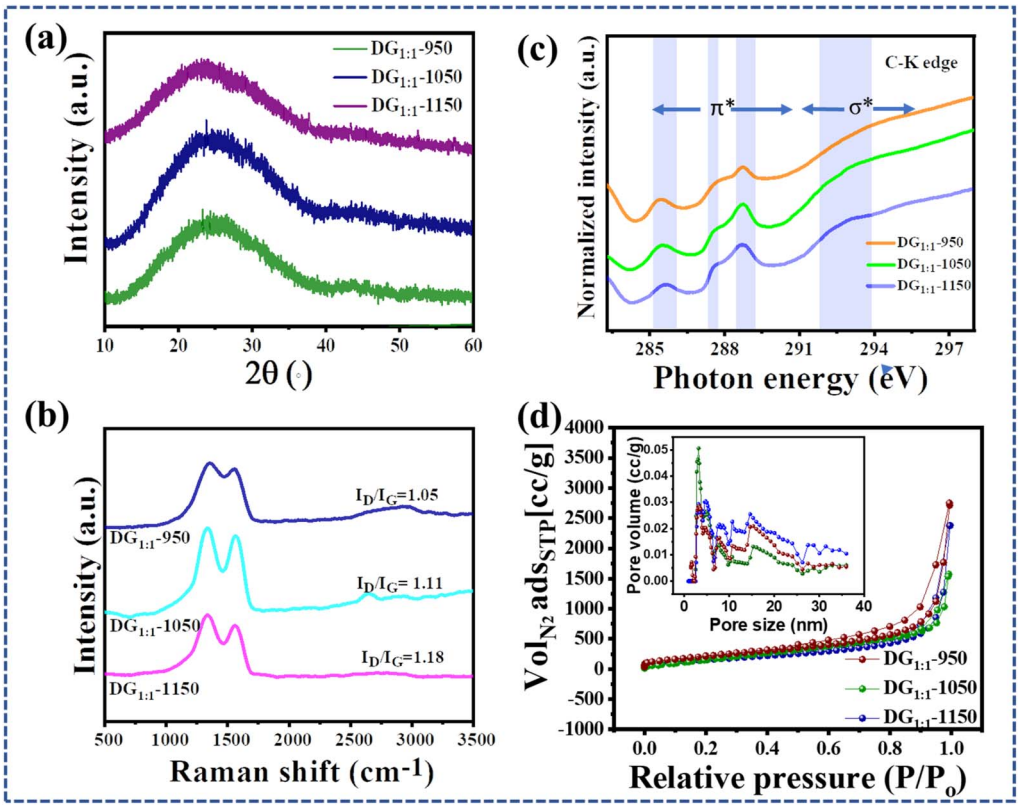

Fig. 3 (a) XRD patterns and (b) Raman spectra of $DG_{1:1}$-950, -1050, and -1150. (c) NEXAFS data: C-K edge. (d) N_2 adsorption–desorption isotherms; inset: the corresponding pore size distribution curves of $DG_{1:1}$-950, -1050, -1150.

much information about the C-speciation related to the D-band feature, such as the hybridization of the carbon atoms in the ring (sp^3 and sp^2). Therefore, near edge X-ray absorption fine structure (NEXAFS) measurements were carried out to investigate the local chemical bonding and electronic structure of the carbon-defect active sites. The C-K edge spectra obtained for all $DG_{1:1}$-*T* samples were found to be similar (Fig. 3c), indicating the similar features of their carbon skeletons. The π^* region is defined as up to ~290 eV and the photon energy range above 290 eV is the σ^* region.[63] The peak at 285.5 eV was assigned to the presence of low coordination carbon atoms at the edges of $DG_{1:1}$-*T* that led to the rehybridization and breakage of integrity of the π-conjugation.[64,65] Therefore, the intensity of the π^* feature decreased as temperature rose and electron transfer to the O_2 molecule is facilitated by the active unpaired π-electrons located at each edge carbon atom. The excitation at 286.2 eV is attributed to N-substituted aromatic carbon and that at 287–288 eV is attributed to C–O/C–OH/C=O.[66]

The specific surface area and porosity of $DG_{1:1}$-*T* were determined by N_2 adsorption and desorption isotherm measurements (Fig. 3d). The Brunauer–Emmett–Teller (BET) specific surface areas for the $DG_{1:1}$-950, -1050 and -1150 samples were found to be 580, 822 and 831 $cm^2\ g^{-1}$, respectively, which shows that the specific surface area increased with an increase in carbonization temperature. The obtained type I isotherm followed by a type IV isotherm with hysteresis suggested the formation of an inter-connected hierarchical porous graphene-like structure spanning both micro- and macropores, further confirmed by the pore size distribution graphs (inset Fig. 3d).[67] The high BET surface area gives a high probability for active site exposure and the hierarchical porous structure can participate more efficiently in the formation of a triple-phase boundary that provides less-resistant diffusion channels for the facile movement of ORR reaction species with the electrolyte and enhances their interactions with catalytically active sites for ORR.[67,68]

That the nitrogen loss by heat treatment is responsible for the defects in the graphene sheets was confirmed by X-ray photoelectron spectroscopy (XPS), as it gives the chemical composition and bonding configuration of the catalyst. The XPS survey spectra (Fig. 4a) confirmed the presence of C, N and O elements in the $DG_{1:1}$-*T*. The fitted high-resolution C 1s spectra indicated residual N and O atoms bonded to the C atoms after annealing, with peaks at about 284.7, 286.07 and 287.8 eV corresponding to C–C, C–N and C=O, respectively, as presented in Fig. S5.†[69] The successful removal of N atoms from the carbon skeleton by annealing was verified by the comparison of deconvoluted N 1s spectra of $DG_{1:1}$-*T* that depict the characteristic peaks for pyridinic N (398.0 eV), pyrrolic N (399.9 eV), graphitic N (401.0 eV) and oxidized N (403.5 eV), as shown in Fig. 4c.[70] However, on annealing at higher temperatures, the signals for N became weak in the XPS pattern.[71] It is clearly represented in the bar diagram (Fig. 4b) that, with the increase in temperature, the N-content decreased from 12.63% to 2.91% and then to 1.36%, resulting in the rise in the formation of defects.[72,73] The comparison bar graph of N-content indicates that the defects are mainly created by the removal of pyridinic and graphitic nitrogen, giving the 5-8-5 or pentagon defects (clearly seen in the STM image) that are highly favorable for ORR activity.[74] Three models have been made based on the N-

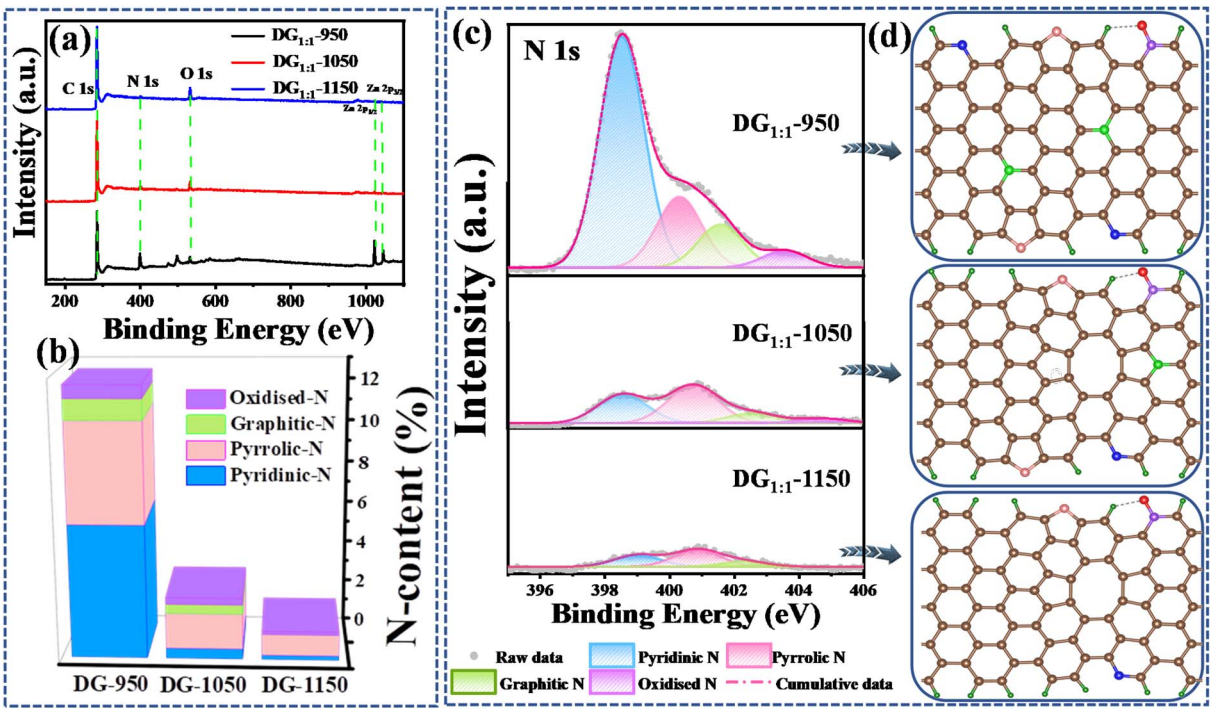

Fig. 4 (a) The wide XPS survey spectra, (b) the bar plot presenting the different N-content in $DG_{1:1}$-950, 1050, 1150, (c) the corresponding deconvoluted N 1s spectra and (d) the correlated models representing N-content and defects in $DG_{1:1}$-950, 1050, 1150.

content obtained from the XPS analysis, as shown in Fig. 4d, and they are similar to theoretical models I, II and III.

It is considered that N dopants, particularly graphitic[24,75] and pyridinic nitrogen,[76,77] can act as active centers for ORR. However, Yao *et al.* presented in their studies that defects are more functional than N in electrocatalytic activity.[22,32,78] Here, we suggest that N and a nearby defect can work synergistically to promote the active sites and the number of active sites also increases due to existence of both extrinsic and intrinsic defects. Optimal concentrations of defects and nitrogen content are required for excellent ORR activity. The presence of N species in the carbon skeleton helps to improve its charge mobility, due to the introduction of electron-donor characteristics, and raises the catalytic activity of carbon in electron-transfer reactions and the abundance of intrinsic defects in the graphene sheet attunes the π electron density in sp^2 carbon systems, providing active sites for ORR.

Electrochemical study

The ORR performances of our synthesized electrocatalysts $DG_{x:y}$-T as a cathode material were investigated in a conventional three electrode system. First, cyclic voltammetry (CV) was performed in Ar and O_2 saturated 0.1 M KOH solution. In the presence of O_2, a reduction peak was obtained for all DG-T which was absent in Ar atmosphere, indicating the electrocatalytic activity of the materials towards ORR (Fig. 5a). The most prominent cathodic peak potential ($E_p = 0.87$ V) was obtained with $DG_{1:1}$ (Fig. S6†) where the ratio of melamine (x) and zinc (y) was 1 : 1 out of $DG_{x:y}$ ($x:y$ = 10 : 1, 2 : 1, 1 : 1 and 1 : 2). The ORR response of the defective carbon only sample $C_{1:1}$ depicts the role of N in addition to that of the defects in the catalyst. The bar graphs (Fig. S7 and S8†) clearly show the optimal conditions for the synthesis of DG (T = 1050 °C and melamine : Zn content = 1 : 1) that exhibited the best ORR performance. To justify the efficiency of $DG_{1:1}$-1050 towards ORR, its activity was compared with those of commercial Pt/C and control DG samples synthesized at different temperatures and with different Zn contents using the RDE technique at 1600 rpm in an O_2 saturated atmosphere. Fig. 5b and S9† provide the evidence that $DG_{1:1}$-1050 outperformed the others with an $E_{1/2} = 0.82$ V, comparable to that of Pt/C ($E_{1/2} = 0.829$ V),[79] and a limiting current density $j_L = 5.7$ mA cm^{-2}, indicating an abundance of exposed active sites that increased the oxygen diffusion rate onto the electrode surface. This good performance can be attributed to the break in electroneutrality and electron transfer due to presence of N dopants around the defects, as they cause charge and spin redistribution in the carbon matrix. ORR is a 4 e^- transfer process. The minimum energy required to lose electrons from the surface of a material is called the work function. For a good electrocatalyst, the work function should be minimal. We performed ultra-violet photoelectron spectroscopy (UPS) to check the electron accessibility due to the N-content and the defects that manipulate the work function of the active sites of $DG_{1:1}$-T for ORR activity. The work function of all three samples was calculated using the equation

$$\phi = h\nu - (E_{\text{cut-off energy}} - E_F) \quad (2)$$

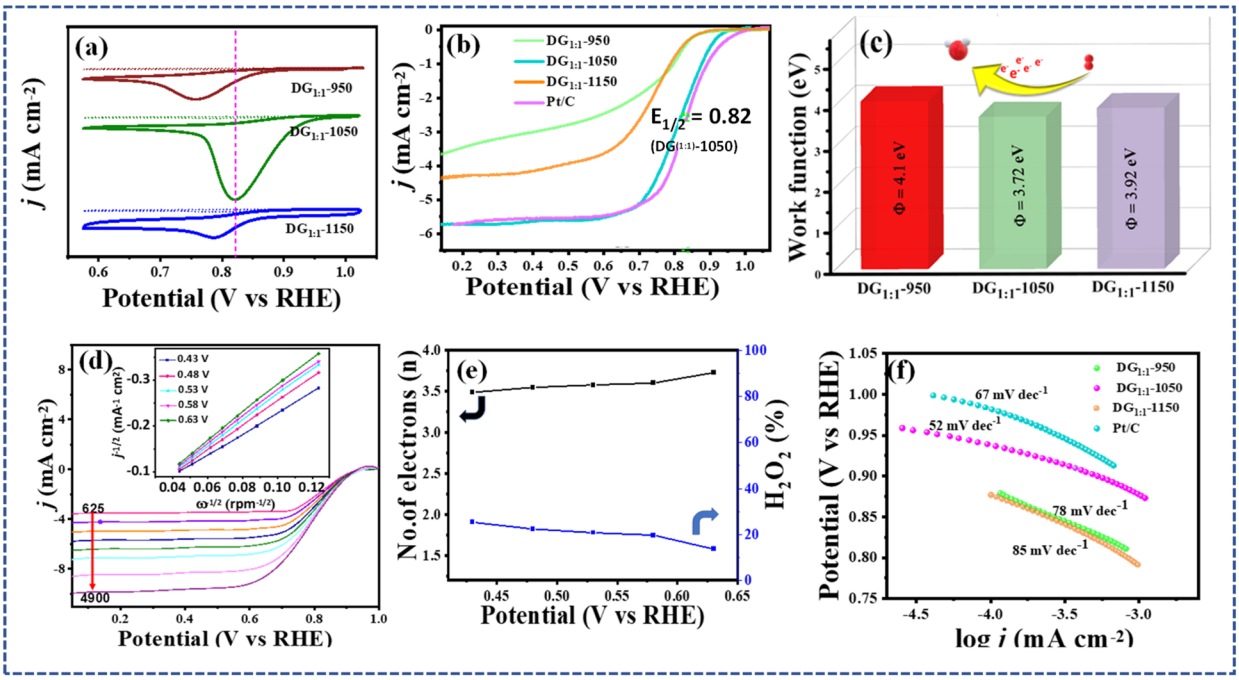

Fig. 5 (a) CV curves of $DG_{1:1}$-950, -1050, -1150 in the presence of Ar (dotted line) and O_2 (solid line); (b) LSV polarization curves of $DG_{1:1}$-950, -1050, -1150 and Pt/C catalyst at 1600 rpm in 0.1 M KOH in saturated with O_2; (c) the bar plot presenting the work functions of $DG_{1:1}$-950, -1050, -1150; (d) LSV curves of $DG_{1:1}$-1050 catalyst at different rotation speeds; (e) H_2O_2 yield and electron transfer number (n) of the $DG_{1:1}$-1050 catalyst in O_2-saturated 0.1 M KOH electrolyte; (f) Tafel plots of $DG_{1:1}$-950, -1050, -1150 and Pt/C, derived from the corresponding LSV curves at 1600 rpm in 0.1 M KOH at 2 mV s^{-1} scan rate.

where ϕ is the work-function of the sample, $h\nu$ denotes the energy of the incident photon of the He (1) source (21.22 eV) and E_F is the energy at the Fermi edge level of the sample, calculated from UPS data (Fig. S10†). The bar diagram shows that the minimum work function (Fig. 5c) was obtained for $DG_{1:1}$-1050 compared to $DG_{1:1}$-950 and 1150 during the ORR process.

From the SVR models, we also found maximum ideal sites for model II. The reaction kinetics were studied using a rotating ring disk electrode (RRDE) under similar conditions by changing the rotation speed of the electrode from 625 to 4900 rpm and using the Koutecky–Levich (K–L) equation (Fig. 5d). The diffusion limiting current density increased with an increase in the speed of rotation due to more diffusion of oxygen and a shortening of the diffusion layer at the electrode surface.[80] Therefore, the obtained K–L plot (inset Fig. 5d) at different potentials (0.43 to 0.63 V) showed linearity and near parallelism that accounted for the first order kinetics of the concentration of dissolved oxygen and the similar number of transferred electrons (n; eqn (4)†) over the whole potential range during the electroreduction of O_2 (Fig. 5e), representing the superior 4 electron transfer in the ORR process. It is noticeable that the catalyst yielded 4 OH^-, which means, following the $4e^-$ transfer kinetics, a negligible number of unwanted intermediates must have formed. The production of H_2O_2 ($2e^-$ process) is an important concern as its decomposition can lead to a chain oxidation reaction due to the formation of highly reactive intermediates.[81] The H_2O_2 yield can be calculated by measuring the ring current using a RRDE system (eqn (5)†). The reduction of peroxide species occurring in the ORR process can be seen from the ring current profile shown in Fig. S11.† The H_2O_2 produced over the potential range is very low (Fig. 5e). The superiority of the activity of $DG_{1:1}$-1050 compared to other control samples and comparability to commercial Pt/C was reinforced by the mass transport corrected Tafel plot drawn from the low overpotential region of LSV at 1600 rpm at a 2 mV s^{-1} scan rate. The Tafel slope of $DG_{1:1}$-1050 was 52 mV dec^{-1}, better than that of Pt/C (64 mV dec^{-1}), as shown in Fig. 5f, presenting fast ORR kinetics with a high electron transfer coefficient and fast first electron transfer from the catalytic site. The low overpotential, high catalytic activity and four-electron pathway were supported by the theoretical calculations. Also, for validation of the SVR model prediction of ΔG_{OH}, we considered the most ideal carbon site number 21 (with predicted $\Delta G_{OH} = 0.36$ eV) in $DG_{1:1}$-1050 (Fig. 6a) and performed DFT calculations for intermediate O, OH, and OOH adsorption. By plotting the free energy profile of ORR (Section S2†) for carbon site 21, we confirmed its lower overpotential and higher catalytic performance (Fig. 6b). The first step of OOH* formation is found to be the potential determining step with an overpotential of 0.45 V at equilibrium potential ($U = 0.4$ V). We also studied the possibility of a two-electron pathway for ORR on site 21 (Section S1e†). In this context, we show that the four-electron pathway is more favorable over the two electron pathway of ORR due to the higher free energy of free OOH/OHOH ion formation than of the O* intermediate (Fig. S12†).

Further, we computed the density of states to investigate the adsorption of ORR intermediates on ideal active site 21 (Fig. S13†). From this, we observed a reduction in the π orbital density of states near the Fermi level after adsorption of O, OH, or OOH, whereas oxygen adsorption occurs through an enolate configuration on site 21 with a large decrease in the density of states near the Fermi level. Later, we confirmed the charge transfer between the active site and the ORR intermediate ions through a Lowdin charge analysis (Fig. S14†). In summary, we unveiled the combined effect of the 5-8-5 defect with N doping and the origin of the higher ORR activity of $DG_{1:1}$-1050 by using π orbital descriptors and the SVR model. The overall mechanism of ORR on active site 21 in $DG_{1:1}$-1050 is shown in Fig. S15.†

Stability and methanol crossover test

Along with the excellent ORR performance, the stability of our catalyst $DG_{1:1}$-1050 was tested at a potential of 0.63 V; it was found to be extremely stable for 12 hours with 98.01% retention

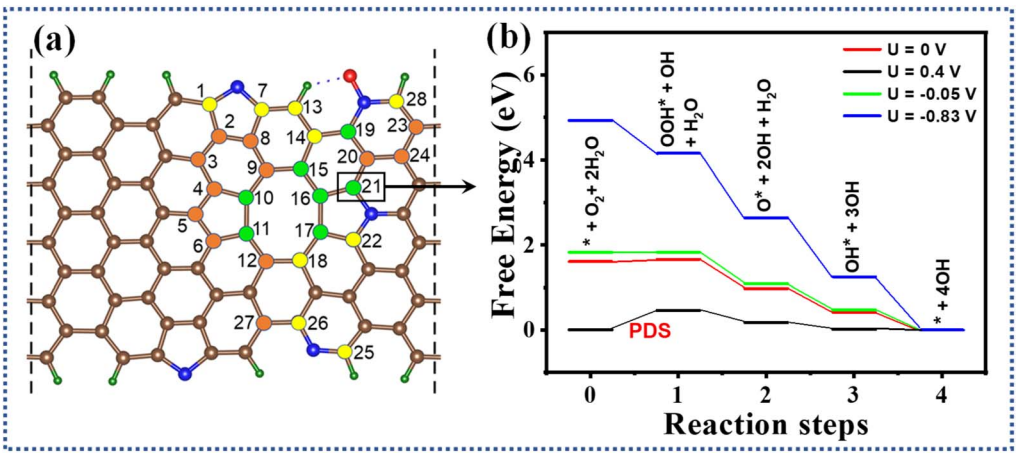

Fig. 6 (a) The optimized model of $DG_{1:1}$-1050 with different active sites and ideal active site (21) for ORR; (b) the free energy profile at different electrode potentials corresponding to site 21 (the first step of OOH* formation is the potential determining step (PDS)) with $\Delta G_{OH} = 0.36$ eV by SVR model prediction and $\Delta G_{OH} = 0.42$ eV by DFT calculations.

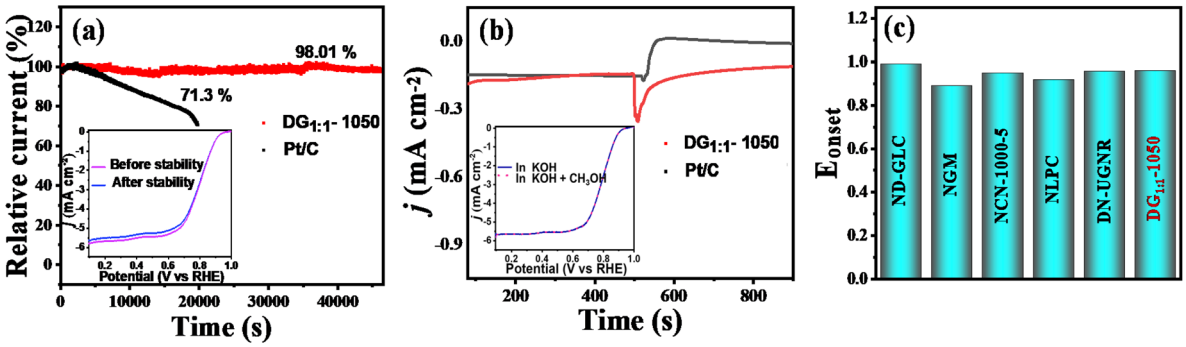

Fig. 7 (a) Chronoamperometric response (i–t) of the $DG_{1:1}$-1050 catalyst and 20 wt% Pt/C at 0.63 V; inset: LSV of $DG_{1:1}$-1050 taken before and after stability in 0.1 M KOH at 1600 rpm. (b) Methanol crossover durability experiment of $DG_{1:1}$-1050 and Pt/C using the chronoamperometric technique in O_2-saturated 0.1 M KOH with addition of 1.0 M CH_3OH solution; inset: LSV of $DG_{1:1}$-1050 taken before and after methanol tolerance in 0.1 M KOH at 1600 rpm. (c) Comparison bar plot of E_{onset} values of N-doped defective carbon catalysts in reported studies.

of initial current density (Fig. 7a), which is superior to other recent reports (Table S4†). The LSVs taken before and after the stability test almost overlay each other (inset Fig. 7a). This result evidenced that there was no mass loss from the electrode that helped to attain non-compromising current density. The facile diffusion of oxygen molecules onto the surface of the electrode with same efficacy was responsible for such stability. The STM done after the stability test (Fig. S16†) also proved the stability of the material. In contrast, there occurred a drop in current density for Pt/C, which may be due to agglomeration of Pt/C nanoparticles leading to less exposure of active sites.[82]

A useful catalyst must have the potential to prevent the possible methanol crossover effect that is a major concern for fuel cell catalysts. To investigate the effect of methanol on our catalyst and Pt/C, the chronoamperometric response was checked after the addition of 1 M CH_3OH in 0.1 M KOH. As seen in Fig. 7b, there occurred almost no change in current density for 850 s for our catalyst, while in the case of Pt/C, an instantaneous increase in current density from negative to positive current was observed after the addition of methanol. The LSVs of $DG_{1:1}$-1050 for ORR taken before and after methanol addition exactly overlaid with each other (inset Fig. 7b). Therefore, the stability of $DG_{1:1}$-1050 in contrast to that of Pt/C against methanol crossover presented the feasibility of its usage as a cathode material in both alkaline and direct methanol fuel cells.

For comparison, all the defective N-doped carbon based electrocatalysts for ORR are summarized in Table S4† and a bar graph in Fig. 7c. $DG_{1:1}$-1050 is found to show similar ORR activity amongst the reported non-metal carbonaceous materials.

Conclusions

In conclusion, we used the QM/ML approach to derive an energy optimized model with both N-atoms and 5-8-5 defect sites that shows superior ORR activity. Following this theoretical result, we adopted a strategy using zinc as a template at 1050 °C to synthesise defective graphene sheets with low N-doping and 5-8-5 defects ($DG_{1:1}$-1050). The formation of defects was visibly confirmed by STM images and variation of N-content was verified by the XPS data. The resulting $DG_{1:1}$-1050 material demonstrates an excellent ORR performance, with onset and half-wave potentials of 0.96 V and 0.82 V, respectively, that is comparable to that of a commercial Pt/C catalyst. The minimal work function of $DG_{1:1}$-1050 determined by UPS further proves its notable ORR performance, as electrons are easily released. Moreover, the DFT study supports the low overpotential and the four-electron pathway. This work paves an important path for the development of metal-free carbon-based nanomaterials for wide application in the fields of energy conversion and storage, with a performance reinforced by the symbiotic effect of optimum defect density and low N-content.

Author contributions

S. Bhardwaj and R. S. Dey designed the work, S. Bhardwaj completed all the experiments and other material characterizations, S. Kapse, R. Thapa did the computational analysis, S. Dan did the STM imaging, S. Bhardwaj and S. Kapse wrote the manuscript, and R. S. Dey supervised the work and corrected the manuscript. All the authors have checked the final version of the manuscript and approved it for submission.

Conflicts of interest

The authors declare no competing financial interest.

Acknowledgements

S. B. acknowledges INST Mohali for providing fellowship and instrumental support. R. S. D. acknowledges DST SERB, India (Grant No. CRG/2020/005683) for financial support. The authors gratefully acknowledge the UGC-DAE-CSR, Indore, for NEXFAS measurements. R. T. thanks DST SERB, India (Grant No. CRG/2021/000620) and National Supercomputer Mission (NSM), India for financial support (Ref No: DST/NSM/R&D_HPC_Applications/2021/19). The authors thank the High-Performance Computing Center, SRM Institute of Science and Technology for providing computational facilities.

References

1 X. Zhou, J. Qiao, L. Yang and J. Zhang, *Adv. Energy Mater.*, 2014, **4**, 1301523.
2 S. Fu, C. Zhu, J. Song, D. Du and Y. Lin, *Adv. Energy Mater.*, 2017, **7**, 1700363.
3 A. Kulkarni, S. Siahrostami, A. Patel and J. K. Nørskov, *Chem. Rev.*, 2018, **118**, 2302–2312.
4 J. Zhang, Z. Zhao, Z. Xia and L. Dai, *Nat. Nanotechnol.*, 2015, **10**, 444–452.
5 S. Guo, P. Yuan, J. Zhang, P. Jin, H. Sun, K. Lei, X. Pang, Q. Xu and F. Cheng, *Chem. Commun.*, 2017, **53**, 9862–9865.
6 Y. Liang, Y. Li, H. Wang, J. Zhou, J. Wang, T. Regier and H. Dai, *Nat. Mater.*, 2011, **10**, 780–786.
7 X. Niu, Y. Li, J. Tang, Y. Hu, H. Zhao and M. Lan, *Biosens. Bioelectron.*, 2014, **51**, 22–28.
8 R. Paul, F. Du, L. Dai, Y. Ding, Z. Lin Wang, F. Wei, A. Roy, R. Paul, F. Du, L. Dai, Y. Ding, Z. L. Wang, F. Wei and A. Roy, *Adv. Mater.*, 2019, **31**, 1805598.
9 C. Lv, Y. Qian, C. Yan, Y. Ding, Y. Liu, G. Chen and G. Yu, *Angew. Chem., Int. Ed.*, 2018, **57**, 10246–10250.
10 X. Liu and L. Dai, *Nat. Rev. Mater.*, 2016, **1**, 16064.
11 H. Liu, Y. Liu and D. Zhu, *J. Mater. Chem.*, 2011, **21**, 3335–3345.
12 C. Huang, C. Li and G. Shi, *Energy Environ. Sci.*, 2012, **5**, 8848–8868.
13 X. K. Kong, C. Le Chen and Q. W. Chen, *Chem. Soc. Rev.*, 2014, **43**, 2841–2857.
14 H. Zhao, C. Sun, Z. Jin, D. W. Wang, X. Yan, Z. Chen, G. Zhu and X. Yao, *J. Mater. Chem. A*, 2015, **3**, 11736–11739.
15 C. Tang, H. F. Wang, X. Chen, B. Q. Li, T. Z. Hou, B. Zhang, Q. Zhang, M. M. Titirici and F. Wei, *Adv. Mater.*, 2016, **28**, 6845–6851.
16 Y. Jia, L. Zhang, A. Du, G. Gao, J. Chen, X. Yan, C. L. Brown and X. Yao, *Adv. Mater.*, 2016, **28**, 9532–9538.
17 Y. Jiang, L. Yang, T. Sun, J. Zhao, Z. Lyu, O. Zhuo, X. Wang, Q. Wu, J. Ma and Z. Hu, *ACS Catal.*, 2015, **5**, 6707–6712.
18 F. Banhart, J. Kotakoski and A. V. Krasheninnikov, *ACS Nano*, 2011, **5**, 26–41.
19 W. J. Lee, J. Lim and S. O. Kim, *Small Methods*, 2017, **1**, 1600014.
20 M. Borghei, J. Lehtonen, L. Liu, O. J. Rojas, E. M. Borghei, J. Lehtonen, O. J. Rojas and L. Liu, *Adv. Mater.*, 2018, **30**, 1703691.
21 H. Yin, P. Yuan, B. A. Lu, H. Xia, K. Guo, G. Yang, G. Qu, D. Xue, Y. Hu, J. Cheng, S. Mu and J. N. Zhang, *ACS Catal.*, 2021, **11**, 12754–12762.
22 X. Zhao, X. Zou, X. Yan, C. L. Brown, Z. Chen, G. Zhu and X. Yao, *Inorg. Chem. Front.*, 2016, **3**, 417–421.
23 X. Wang, Y. Jia, X. Mao, L. Zhang, D. Liu, L. Song, X. Yan, J. Chen, D. Yang, J. Zhou, K. Wang, A. Du and X. Yao, *Chem*, 2020, **6**, 2009–2023.
24 X. Lu, D. Wang, L. Ge, L. Xiao, H. Zhang, L. Liu, J. Zhang, M. An and P. Yang, *New J. Chem.*, 2018, **42**, 19665–19670.
25 C. V. Rao, C. R. Cabrera and Y. Ishikawa, *J. Phys. Chem. Lett.*, 2010, **1**, 2622–2627.
26 L. Lai, J. R. Potts, D. Zhan, L. Wang, C. K. Poh, C. Tang, H. Gong, Z. Shen, J. Lin and R. S. Ruoff, *Energy Environ. Sci.*, 2012, **5**, 7936–7942.
27 Z. Zhang, L. Yu, Y. Tu, R. Chen, L. Wu, J. Zhu and D. Deng, *Cell Rep. Phys. Sci.*, 2020, **1**, 100145.
28 X. Xue, H. Yang, T. Yang, P. Yuan, Q. Li, S. Mu, X. Zheng, L. Chi, J. Zhu, Y. Li, J. Zhang and Q. Xu, *J. Mater. Chem. A*, 2019, **7**, 15271–15277.
29 K. Gong, F. Du, Z. Xia, M. Durstock and L. Dai, *Science*, 2009, **323**, 760–764.
30 Y. Jiang, L. Yang, T. Sun, J. Zhao, Z. Lyu, O. Zhuo, X. Wang, Q. Wu, J. Ma and Z. Hu, *ACS Catal.*, 2015, **5**, 6707–6712.
31 J. Zhang, T. Wang, P. Liu, S. Liu, R. Dong, X. Zhuang, M. Chen and X. Feng, *Energy Environ. Sci.*, 2016, **9**, 2789–2793.
32 Y. Jia, L. Zhang, A. Du, G. Gao, J. Chen, X. Yan, C. L. Brown and X. Yao, *Adv. Mater.*, 2016, **28**, 9532–9538.
33 S. Sinthika and R. Thapa, *RSC Adv.*, 2015, **5**, 93215–93225.
34 S. Sinthika, U. V. Waghmare and R. Thapa, *Small*, 2018, **14**, 1703609.
35 P. Marbaniang, S. Kapse, S. Ingavale, R. Thapa and B. Kakade, *Int. J. Energy Res.*, 2021, **45**, 21293–21306.
36 S. Kapse, N. Barman and R. Thapa, *Carbon*, 2023, **201**, 703–711.
37 P. Marbaniang, S. Kapse, S. Ingavale, R. Thapa and B. Kakade, *Int. J. Energy Res.*, 2021, **45**, 21293–21306.
38 S. Sinthika and R. Thapa, *RSC Adv.*, 2015, **5**, 93215–93225.
39 S. Kapse, N. Barman and R. Thapa, *Carbon*, 2023, **201**, 703–711.
40 X. Zhu, J. Yan, M. Gu, T. Liu, Y. Dai, Y. Gu and Y. Li, *J. Phys. Chem. Lett.*, 2019, **10**, 7760–7766.
41 M. Rück, B. Garlyyev, F. Mayr, A. S. Bandarenka and A. Gagliardi, *J. Phys. Chem. Lett.*, 2020, **11**, 1773–1780.
42 H. Zhao, C. Sun, Z. Jin, D. W. Wang, X. Yan, Z. Chen, G. Zhu and X. Yao, *J. Mater. Chem. A*, 2015, **3**, 11736–11739.
43 K. Yang, J. Zaffran and B. Yang, *Phys. Chem. Chem. Phys.*, 2021, **23**, 4454.
44 Z. Zhao, M. Li, L. Zhang, L. Dai and Z. Xia, *Adv. Mater.*, 2015, **27**, 6834–6840.
45 Y. Jiao, Y. Zheng, M. Jaroniec and S. Z. Qiao, *J. Am. Chem. Soc.*, 2014, **136**, 4394–4403.
46 J. Zhang, Z. Zhao, Z. Xia and L. Dai, *Nat. Nanotechnol.*, 2015, **10**, 444–452.
47 H. Sun, M. Wang, X. Du, Y. Jiao, S. Liu, T. Qian, Y. Yan, C. Liu, M. Liao, Q. Zhang, L. Meng, L. Gu, J. Xiong and C. Yan, *J. Mater. Chem. A*, 2019, **7**, 20952–20957.
48 H. Tao, S. Liu, J. L. Luo, P. Choi, Q. Liu and Z. Xu, *J. Mater. Chem. A*, 2018, **6**, 9650–9656.
49 J. H. Zagal and M. T. M. Koper, *Angew. Chem., Int. Ed.*, 2016, **55**, 14510–14521.
50 S. Sinthika, U. V. Waghmare and R. Thapa, *Small*, 2018, **14**, 1–10.
51 J. Ma, Q. Zhi, L. Gong, Y. Shen, D. Sun, Y. Guo, L. Zhang and Z. Xia, *Nanoscale*, 2020, **12**, 19375–19382.
52 S. Kapse, S. Janwari, U. V. Waghmare and R. Thapa, *Appl. Catal., B*, 2021, **286**, 119866.

53 P. Marbaniang, S. Kapse, S. Ingavale, R. Thapa and B. Kakade, *Int. J. Energy Res.*, 2021, **45**, 21293–21306.
54 S. Lim, K. Suh, Y. Kim, M. Yoon, H. Park, D. N. Dybtsev and K. Kim, *Chem. Commun.*, 2012, **48**, 7447–7449.
55 Q. Cheng, C. Hu, G. Wang, Z. Zou, H. Yang and L. Dai, *J. Am. Chem. Soc.*, 2020, **142**, 5594–5601.
56 W. Zhang, Z. Y. Wu, H. L. Jiang and S. H. Yu, *J. Am. Chem. Soc.*, 2014, **136**, 14385–14388.
57 L. Ye, G. Chai and Z. Wen, *Adv. Funct. Mater.*, 2017, **27**, 1606190.
58 H. Zhao, C. Sun, Z. Jin, D. W. Wang, X. Yan, Z. Chen, G. Zhu and X. Yao, *J. Mater. Chem. A*, 2015, **3**, 11736–11739.
59 D. Ye, L. Wang, R. Zhang, B. Liu, Y. Wang and J. Kong, *J. Mater. Chem. A*, 2015, **3**, 15171–15176.
60 Y. Zheng, Y. Jiao, J. Chen, J. Liu, J. Liang, A. Du, W. Zhang, Z. Zhu, S. C. Smith, M. Jaroniec, G. Q. Lu and S. Z. Qiao, *J. Am. Chem. Soc.*, 2011, **133**, 20116–20119.
61 J. Zhang, Y. Sun, J. Zhu, Z. Kou, P. Hu, L. Liu, S. Li, S. Mu and Y. Huang, *Nano Energy*, 2018, **52**, 307–314.
62 N. Kamboj, T. Purkait, M. Das, S. Sarkar, K. S. Hazra and R. S. Dey, *Energy Environ. Sci.*, 2019, **12**, 2507–2517.
63 N. Gallagher, H. Zhang, T. Junghoefer, E. Giangrisostomi, R. Ovsyannikov, M. Pink, S. Rajca, M. B. Casu and A. Rajca, *J. Am. Chem. Soc.*, 2019, **141**(11), 4764–4774.
64 Y. Zheng, Y. Jiao, Y. Zhu, L. H. Li, Y. Han, Y. Chen, M. Jaroniec and S. Z. Qiao, *J. Am. Chem. Soc.*, 2016, **138**, 16174–16181.
65 Y. Zheng, Y. Jiao, Y. Zhu, L. H. Li, Y. Han, Y. Chen, A. Du, M. Jaroniec and S. Z. Qiao, *Nat. Commun.*, 2014, **5**, 2–9.
66 J. Lehmann, D. Solomon, J. Brandes, H. Fleckenstein, C. Jacobson and J. Thieme, in *Biophysico-Chemical Processes Involving Natural Nonliving Organic Matter in Environmental Systems*, ed. N. Senesi, B. Xing and P. M. Huang, John Wiley & Sons, Inc., N. J. Hoboken, USA, 2009, ch. 17, pp. 729–781.
67 J. Zhang, H. Zhou, J. Zhu, P. Hu, C. Hang, J. Yang, T. Peng, S. Mu and Y. Huang, *ACS Appl. Mater. Interfaces*, 2017, **9**, 24545–24554.
68 M. Borghei, J. Lehtonen, L. Liu and O. J. Rojas, *Adv. Mater.*, 2018, **30**, 1703691.
69 N. Kamboj, B. Debnath, S. Bhardwaj, T. Paul, N. Kumar, S. Ogale, K. Roy and R. S. Dey, *ACS Nano*, 2022, **16**, 15358–15368.
70 K. Khan, T. Liu, M. Arif, X. Yan, M. D. Hossain, F. Rehman, S. Zhou, J. Yang, C. Sun, S. H. Bae, J. Kim, K. Amine, X. Pan and Z. Luo, *Adv. Energy Mater.*, 2021, **11**, 2101619.
71 Q. Ren, H. Wang, X. F. Lu, Y. X. Tong and G. R. Li, *Adv. Sci.*, 2018, **5**, 1700515.
72 Y. Chang, F. Hong, C. He, Q. Zhang and J. Liu, *Adv. Mater.*, 2013, **25**, 4794–4799.
73 D. Li, Y. Jia, G. Chang, J. Chen, H. Liu, J. Wang, Y. Hu, Y. Xia, D. Yang and X. Yao, *Chem*, 2018, **4**, 2345–2356.
74 R. Ma, G. Lin, Y. Zhou, Q. Liu, T. Zhang, G. Shan, M. Yang and J. Wang, *npj Comput. Mater.*, 2019, **5**, 78.
75 N. Wang, B. Lu, L. Li, W. Niu, Z. Tang, X. Kang and S. Chen, *ACS Catal.*, 2018, **8**, 6827–6836.
76 L. Lai, J. R. Potts, D. Zhan, L. Wang, C. K. Poh, C. Tang, H. Gong, Z. Shen, J. Lin and R. S. Ruoff, *Energy Environ. Sci.*, 2012, **5**, 7936–7942.
77 C. V. Rao, C. R. Cabrera and Y. Ishikawa, *J. Phys. Chem. Lett.*, 2010, **1**, 2622–2627.
78 X. Yan, Y. Jia, T. Odedairo, X. Zhao, Z. Jin, Z. Zhu and X. Yao, *Chem. Commun.*, 2016, **52**, 8156–8159.
79 S. Chen, L. Zhao, J. Ma, Y. Wang, L. Dai and J. Zhang, *Nano Energy*, 2019, **60**, 536–544.
80 S. Sarkar, N. Kamboj, M. Das, T. Purkait, A. Biswas and R. S. Dey, *Inorg. Chem.*, 2020, **59**, 1332–1339.
81 N. Ramaswamy, N. Hakim and S. Mukerjee, *Electrochim. Acta*, 2008, **53**, 3279–3295.
82 X. Cui, S. Yang, X. Yan, J. Leng, S. Shuang, P. M. Ajayan and Z. Zhang, *Adv. Funct. Mater.*, 2016, **26**, 5708–5717.